HEALTH AND MEDICINE

Stem cell–homing biomimetic hydrogel promotes the repair of osteoporotic bone defects through osteogenic and angiogenic coupling

Fei-Long Wei[1,2]†, Yuan Zhai[3]†, Tian-Fu Wang[1]†, Jing-Wei Zhao[1]†, Chao-Li Wang[4], Zhen Tang[1], Kuo Shen[5], Hao Wu[1], Rui Zheng[6], Ming-Rui Du[1], Wei Heng[1], Xiao-Xiang Li[1], Xiao-Dong Yan[1], Quan-You Gao[1]*, Zheng Guo[1], Ji-Xian Qian[1]*, Cheng-Pei Zhou[1]*

Osteoporotic bone defects refer to the disruption of bone structural integrity in patients with osteoporosis and pose a substantial challenge to orthopedic surgeons. In this study, we developed a biomimetic hydrogel to improve the osteogenic microenvironment and promote stem cell homing. This hydrogel served as a container for S-nitrosoglutathione and Ca^{2+}, promoting the release of bioactive nitric oxide (NO) from bone marrow mesenchymal stem cells (BMSCs) and human vascular endothelial cells and activating the NO/cyclic guanosine monophosphate signaling pathway. These changes promote osteogenic and angiogenic couplings. The hydrogel simultaneously recruited BMSCs by conjugating the stem cell homing peptide SKPPGTSS. Using a rat distal femoral defect model, it was demonstrated that this hydrogel can effectively increase the formation of bone tissue and new blood vessels and has immune-regulating functions. We envision that this hydrogel may be a minimally invasive yet highly effective strategy for expediting the healing of osteoporotic bone defects.

INTRODUCTION

More than 200 million people worldwide suffer from osteoporosis, a systemic disorder of bone metabolism characterized by bone loss, changes in bone microstructure, and fragility fractures (*1, 2*). Osteoporotic bone defects refer to the disruption of bone structural integrity in patients with osteoporosis, often resulting from trauma, surgery to remove tumors, or infections (*3*). In clinical practice, autologous bone remains the gold-standard treatment for bone defects (*4*). However, the efficacy of this therapeutic modality is constrained by potential complications that may manifest at the donor site and the limited availability of resources (*5*). Considering these clinical requirements, alternative strategies for bone tissue regeneration have been devised (*3, 5*).

A healthy vascular condition and generation of new blood vessels can provide sufficient nutrition for bone development and fracture healing (*6*). A distinct type of blood vessel in the skeletal system, named CD31^{hi}Emcn^{hi}, or type H blood vessels, mediates the differentiation of perivascular osteoblasts and integrates angiogenesis with osteogenesis (*7*). However, osteoporosis results in a reduction in the number of H-type endothelial cells (*8*). Nitric oxide (NO) is an endogenous gas-signaling molecule that regulates numerous physiological processes (*9–11*). It promotes regeneration and prevents the calcification of biohybrid vascular grafts by modulating vascular stem/progenitor cells (*12*).

Furthermore, NO promotes osteogenesis in bone marrow mesenchymal stem cells (BMSCs) by activating the NO/cyclic guanosine monophosphate (cGMP) signaling pathway (*6*). However, NO is not targeted, making it challenging for NO donors to enter specific cells and play a role. The biomedical applications of mesoporous silica nanoparticles (MSNs) are growing owing to their desirable properties, including their large surface area, high loading capacity, and biocompatibility (*13*). To enhance the therapeutic efficacy, monodisperse silica has been proposed to deliver different biomolecules to treat diseases (*14, 15*). Mora-Raimundo *et al.* (*15, 16*) used MSNs for intracellular delivery of nucleic acids to treat osteoporosis with positive outcomes. Previously, we successfully developed biomimetic nanomaterials for treating spinal cord injuries using MSNs (*17*). Here, we designed MSNs to carry S-nitrosoglutathione (GSNO) to supply NO to cells. In addition, BMSCs and human vascular endothelial cells (HUVECs) cell membranes (CMs) are wrapped on the surface of MSNs to target them.

Recent studies have demonstrated that the extracellular matrix consists of a three-dimensional (3D) network that facilitates cell adhesion, migration, and proliferation, as well as oxygen and nutrient exchange, and plays an indispensable role in bone repair. Furthermore, bone-substitute biomaterials must have good intraoperative handling properties (*18*). Consequently, substantial attention has been devoted to injectable composite biomaterials for bone regeneration (*5, 18*). The 3D hydrophilic networks and high water content distinguish the hydrogels as distinct scaffold materials. This composition closely resembled that of normal interstitial cells (*19*). Sodium alginate (SA) hydrogels have been approved by the US Food and Drug Administration because of their excellent biocompatibility (*20*). However, because SA lacks cell adhesion sites, covalent modifications are usually applied to it (*21*). In this study, we covalently modified SA to enhance cell/matrix interactions for better adhesion.

Moreover, recruiting BMSCs to differentiate into new osteoblasts is crucial for repairing bone defects. On the basis of its structural similarity to the bone marrow–homing peptide (BMHP), the short peptide sequence SKPPGTSS promoted the homing of mesenchymal

[1]Department of Orthopaedics, Tangdu Hospital, Fourth Military Medical University, 710038 Xi'an, China. [2]Department of Orthopaedics, General Hospital of Central Theater Command (Wuhan General Hospital of Guangzhou Command, previously), Wuhan 430030, China. [3]Basic Medical College, Fourth Military Medical University, Xi'an 710032, China. [4]Department of Pharmaceutical Analysis, School of Pharmacy, Fourth Military Medical University, Xi'an 710032, China. [5]Department of Burns and Cutaneous Surgery, Xijing Hospital, Fourth Military Medical University, 710032 Xi'an, China. [6]State Key Laboratory of Holistic Integrative Management of Gastrointestinal Cancers, Department of Biochemistry and Molecular Biology, Fourth Military Medical University, Xi'an, Shaanxi 710032, China.
*Corresponding author. Email: zhoucpei@fmmu.edu.cn (C.-P.Z.); pasmiss2012@163.com (J.-X.Q.); guozheng@fmmu.edu.cn (Z.G.); 18009129090@163.com (Q.-Y.G.)
†These authors contributed equally to this work.

stem cells. The hydrogel served as a platform for BMSCs homing through SKPPGTSS engraftment (*22*, *23*).

BMSCs also contribute to tissue repair through their paracrine effect (*24*). BMSCs secrete various cytokines and growth factors that regulate various physiological functions, including angiogenesis (*25*), immune regulation (*26*), and cell differentiation (*27*). BMSCs are highly sensitive to environmental changes. Lin *et al.* (*25*) revealed that matrix stiffness can affect the paracrine function of BMSCs. The stiffness of the SA hydrogel exhibits a linear relationship with the number of divalent cations. Its internal structure is typical of an egg box and remains unaffected by changes in the concentration of chelated divalent cations (*28*). In this study, we changed the SA stiffness using calcium ions to improve the paracrine properties of BMSCs. In summary, we have developed a biomimetic nanomaterial that promotes the coupling

of osteogenesis and angiogenesis and has immunomodulatory functions (Fig. 1).

RESULTS

BMSCs from osteoporotic rat exhibits properties associated with aging

The senescence, stemness, and osteogenic potential of the BMSCs were investigated to understand their properties better. Micro–computed tomography (micro-CT) results revealed that the volume, thickness, and number of trabecular bones were significantly reduced in ovariectomized middle-aged rats (Fig. 2A). Hematoxylin and eosin (H&E) and Masson staining demonstrated notable osteoporosis in ovariectomized middle-aged rats (Fig. 2, B and C). As illustrated in
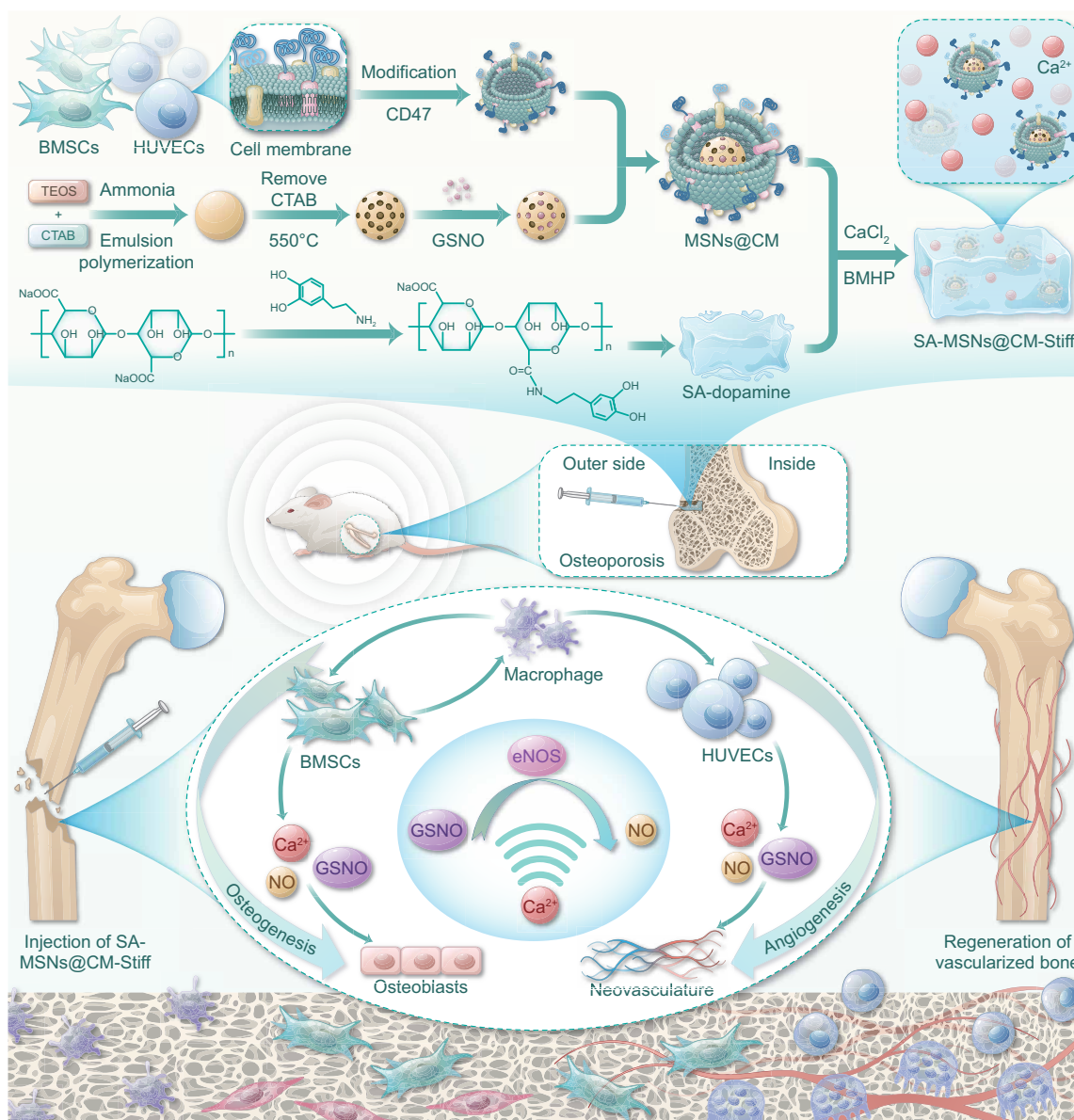

Fig. 1. Schematic of SA-MSNs@CM-Stiff for osteoporotic bone defects. A biomimetic nanomaterial that promotes the coupling of osteogenesis and angiogenesis and has immunomodulatory functions. CTAB, Hexadecyltrimethylammonium bromide.
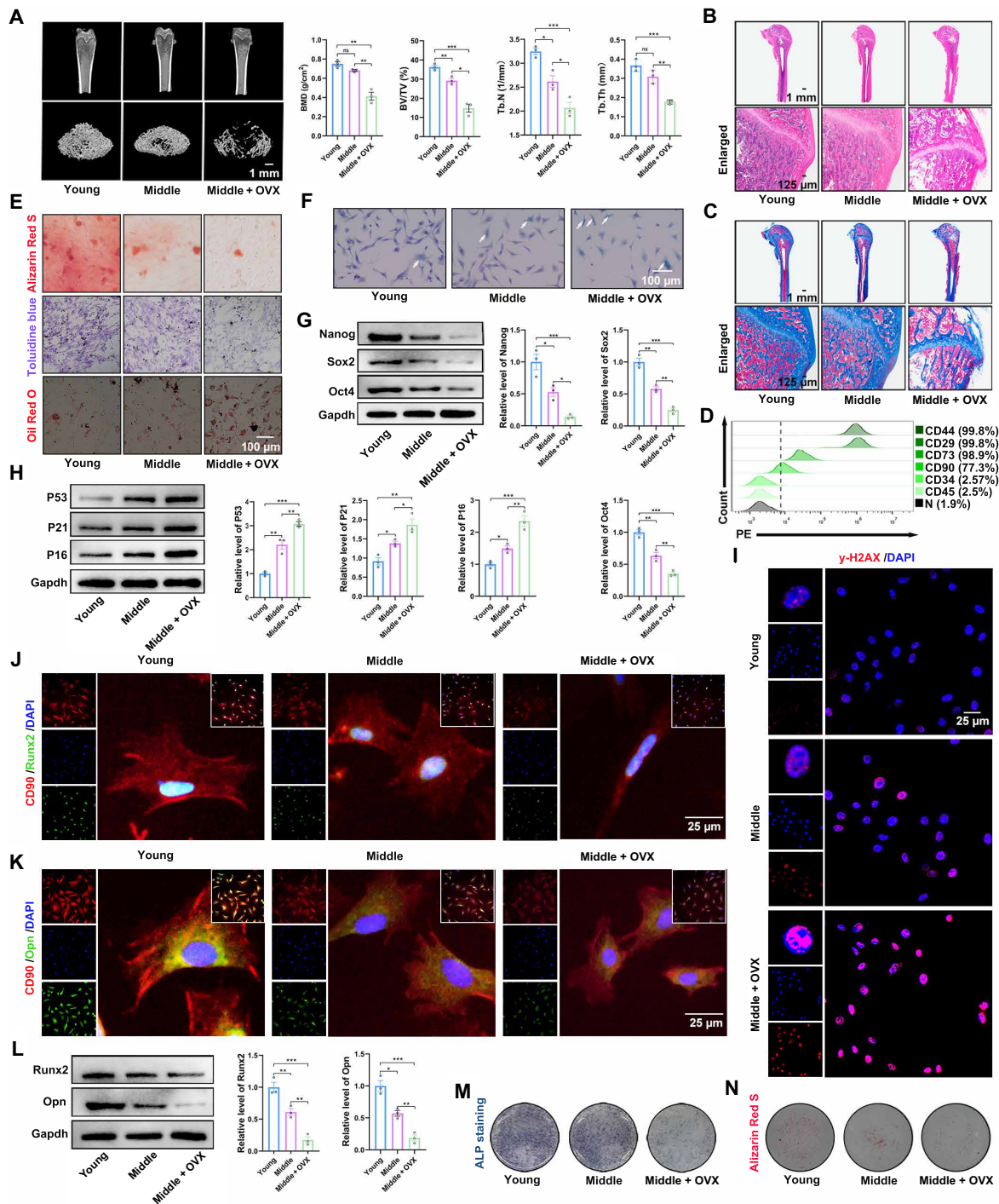
Fig. 2. BMSCs from osteoporotic rats show properties associated with aging. (**A**) Micro-CT scan and 3D reconstruction results (scale bar, 1 mm); quantitative analysis of bone density, volume, and other parameters. BV/TV, bone tissue volume/total tissue; Tb.Th, trabecular thickness; Tb.N, trabecular number. (**B**) H&E staining images of different groups (scale bar, 1 mm and 125 μm). (**C**) Masson staining images of different groups (scale bar, 1 mm and 125 μm). (**D**) Flow cytometry showed BMSCs from osteoporotic rats were positive for CD44 (99.8%), CD29 (99.8%), CD73 (98.9%), and CD90 (77.3%) and negative for CD34 (2.57%) and CD45 (2.5%). (**E**) Alizarin Red S, Toluidine blue, and Oil Red O staining were used to detect osteogenic, chondrogenic, and adipogenic differentiation, respectively (scale bar, 100 μm). (**F**) SA-β-gal staining detected senescent cells (scale bar, 100 μm). (**G**) Western blotting analysis of Nanog, Sox2, and Oct4 protein expression in BMSCs from different groups. (**H**) Western blotting analysis of P53, P21, and P16 protein expression in BMSCs from different groups. (**I**) Representative immunofluorescence staining of γ-H2AX foci formation in BMSCs from different groups (scale bar, 25 μm). DAPI, 4′,6-diamidino-2-phenylindole. (**J**) Representative immunofluorescence staining of CD90 and Runx2 in BMSCs from the different groups (scale bar, 25 μm). (**K**) Representative immunofluorescence staining of CD90 and Opn in BMSCs from different groups (scale bar, 25 μm). (**L**) Western blotting analysis of Runx2 and Opn protein expression in BMSCs from different groups. (**M**) ALP staining of BMSCs from the different groups. (**N**) Alizarin Red S staining of BMSCs from different groups. $n = 3$ for each group. Error bars denote means ± SEM; ns, no significance; *$P < 0.05$, **$P < 0.01$, and ***$P < 0.001$.

Fig. 2D, the BMSCs exhibited positive expression of the mesenchymal stem cell surface markers CD44, CD29, CD73, and CD90. In contrast, the expression levels of CD34 and CD45 were negligible (Fig. 2D and fig. S1, A and B). BMSCs were isolated from the femurs of young, middle-aged, and middle-aged ovariectomized rats and were identified through three-way differentiation. The osteogenic and chondrogenic abilities of osteoporotic rats were notably reduced, and their adipogenic abilities were notably increased (Fig. 2E). As anticipated, BMSCs from osteoporotic rats exhibited more SA-β-gal–positive cells than young or middle-aged rats (Fig. 2F). A significant difference was also observed in the expression levels of Nanog, Sox2, and Oct4 in the osteoporosis group compared to the young and middle-aged groups (Fig. 2G). Subsequently, we identified senescence-related factors, such as P53, P21, and P16 (29). A significant increase in these senescence-related factors was observed in BMSCs from osteoporotic rats (Fig. 2H). Senescence is also characterized by a persistent DNA damage response commonly detecting γ-H2AX foci (29). The osteoporosis group exhibited more γ-H2AX–positive foci (Fig. 2I). Moreover, the osteogenic potential of the BMSCs was evaluated. The expression of osteogenic marker proteins (Runx2 and Opn) was decreased in the osteoporosis group compared to that in the young and middle-aged groups (Fig. 2, J to L). Alkaline phosphatase (ALP) staining indicated that the osteoporosis group was lighter than the young and middle-aged groups (Fig. 2M). Furthermore, the osteoporosis group calcium nodules were smaller (Fig. 2N). In conclusion, the osteogenic ability of BMSCs is significantly reduced in osteoporotic rats.

Characteristics of synthesized MSNs, MSNs@CM, SA, SA-MSNs@CM, and SA-MSNs@CM-Stiff

To address the issue of the poor repair ability of osteoporotic bone defects, we designed a biomimetic hydrogel with a stem cell–homing effect. Four steps were involved in preparing membrane-biomimetic MSNs@CM: Synthesis of MSNs was the first step; then GSNO was adsorbable to mesoporous channels in MSNs; the third step consisted of ultracentrifuging BMSCs and HUVECs to extract CM; and last, extrusion coated the pre-extracted CM onto the nanoparticle surfaces, resulting in MSNs@CM (Fig. 1). Figure 3A presents the transmission electron microscopy (TEM) images of the MSNs and MSNs@CM. The MSNs had their dimensions of 197.6 nm, whereas MSNs@CM were 229.8 nm (Fig. 3B). Furthermore, the zeta potential of MSNs was −27.2 mV, and MSNs@CM was −25.85 mV (Fig. 3C). Flow cytometry results showed that CM coverage facilitated the entry of MSNs into cells (fig. S2, A and B). However, long-term maintenance of MSNs at defective sites is challenging. Our solution was to design an SA hydrogel–based delivery system that could prolong the retention of GSNO at the defect site (Fig. 1). However, because SA lacks cell adhesion sites, it is usually covalently modified with ligands to provide cell adhesion sites. In this study, the SA backbone molecule was covalently bound to dopamine (Fig. 3D). In the cell adhesion experiments, $\frac{1}{50}$ dopamine binding enabled more cells to adhere (Fig. 3, E and F). The N1s signal, absent in SA, was detected using x-ray photoelectron spectroscopy (XPS), thus proving the effective grafting of dopamine (Fig. 3G). SA hydrogels with distinct mechanical properties can be prepared by adjusting the molar concentration of divalent cations (Fig. 3H). The groups were named 20, 30, 40, 50, and 60 mM according to the concentration of calcium ions in each group (Fig. 3I). Compression experiments were conducted to determine the initial elastic moduli of the hydrogels. The elastic modulus of the gel increased as the Ca^{2+} molar concentration in the gel increased and reached a maximum value of 25.56 ± 1.41 kPa at 50 mM

(Fig. 3I). Consequently, we used the 50 mM group as the stiffening SA hydrogel group. To observe the internal microstructures of the different groups, we photographed freeze-dried samples using a scanning electron microscope. The internal structures of the groups did not differ notably (Fig. 3J). The pore diameters of SA, SA-MSNs@CM, and SA-MSNs@CM-Stiff groups were 181.49 ± 59.47, 164.69 ± 48.99, and 170.01 ± 55.04 μm, respectively (Fig. 3K). There was no notable difference in pore size among different groups. Low-frequency nuclear magnetic resonance testing yielded similar results (fig. S3). The mechanical properties and adhesion capabilities of SA-MSNs@CM-Stiff exhibited flexibility and softness under different external mechanical forces, such as bending and stretching (Fig. 3L). Using hydrogels to prepare complex 3D tissue scaffolds has recently attracted widespread attention and is expected to be useful in the precise and personalized treatment of bone defects. The SA-MSNs@CM-Stiff hydrogel exhibited good processing properties and was easily obtained in various shapes (Fig. 3M).

SA-MSNs@CM-Stiff promotes osteogenesis by activating the NO/cGMP pathway in vitro

BMSCs were cocultured with different hydrogel groups via indirect contact. First, the biocompatibility of the hydrogels was determined. The findings indicated that the SA-MSNs@CM and SA-MSNs@CM-Stiff groups maintained the cells in a better-spreading state (Fig. 4A). Calcein-AM/propidium iodide (PI) staining demonstrated that various hydrogel groups exhibited good biocompatibility (Fig. 4B). We then tested whether a sustained and sufficient supply of GSNO and Ca^{2+} could synergistically promote NO production and stimulate downstream signaling. A significant increase in phospho-endothelial nitric oxide synthase (P-eNOS) expression was observed in BMSCs of the SA-MSNs@CM and SA-MSNs@CM-Stiff groups after 7 days of coculture (Fig. 4C). Similarly, NO levels also increased significantly in the SA-MSNs@CM and SA-MSNs@CM-Stiff groups (Fig. 4D). Moreover, a significant increase in downstream signaling molecules, such as cGMP, soluble guanylate cyclase (sGC), and protein kinase G (PKG), was observed in the SA-MSNs@CM and SA-MSNs@CM-Stiff groups (Fig. 4, E and F). Xu et al. (6) demonstrated that NO promotes osteogenesis. We examined the effect of elevated NO levels on osteogenesis. Western blotting analysis revealed that Runx2 and Opn were significantly upregulated in the SA-MSNs@CM and SA-MSNs@CM-Stiff groups (Fig. 4G). Immunofluorescence experiments yielded similar results (Fig. 4, H and I). ALP staining demonstrated that SA-MSNs@CM and SA-MSNs@CM-Stiff were darker than SA and the control (Fig. 4J). Furthermore, larger calcium nodules were observed in the SA-MSNs@CM and SA-MSNs@CM-Stiff groups (Fig. 4K). These findings indicate that SA-MSNs@CM and SA-MSNs@CM-Stiff could activate the NO/cGMP pathway to stimulate osteogenesis in BMSCs (Fig. 4L).

SA-MSNs@CM-Stiff promotes migration and angiogenesis by activating the NO/cGMP pathway in vitro

HUVECs were cocultured with different hydrogel groups through indirect contact. First, the biocompatibility of the hydrogels was determined. The results revealed that the SA-MSNs@CM and SA-MSNs@CM-Stiff groups maintained the cells in a better-spreading state (Fig. 5A). Calcein-AM/PI staining revealed good biocompatibility of the different groups of hydrogels (Fig. 5B). We then tested whether a sustained and sufficient supply of GSNO and Ca^{2+} could synergistically promote NO production and stimulate downstream signaling in HUVECs. P-eNOS expression was significantly increased in HUVECs of the SA-MSNs@CM and SA-MSNs@CM-Stiff groups after 3 days of
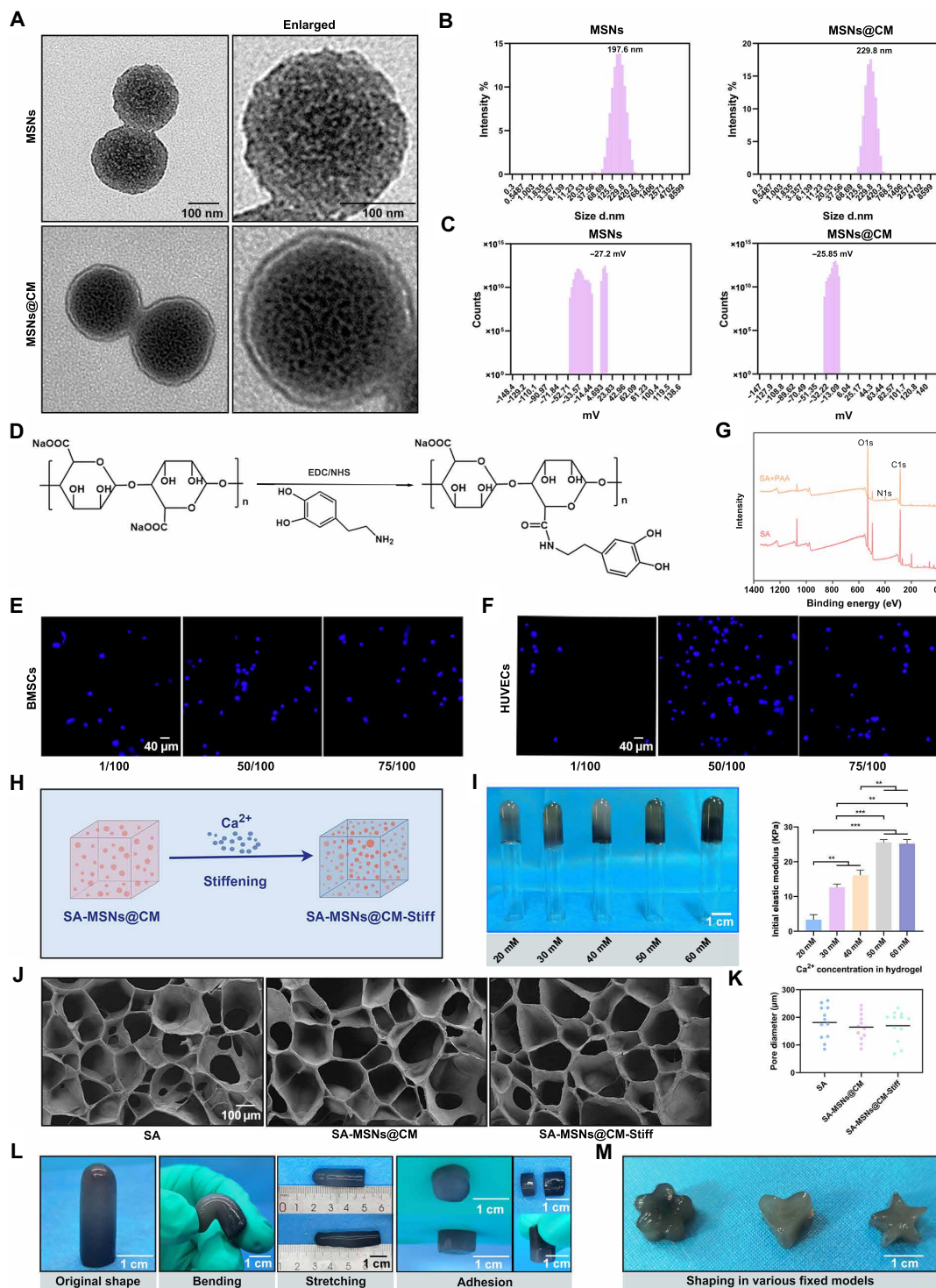
Fig. 3. Characteristics of Synthesized MSNs, SA, SA-MSNs@CM, and SA-MSNs@CM-Stiff. (**A**) TEM images of MSNs and MSNs@CM (scale bar, 100 nm). (**B**) Size distribution of MSNs and MSNs@CM. (**C**) Zeta potential distribution of MSNs and MSNs@CM. (**D**) Schematic diagram of dopamine grafting in SA. (**E**) Nuclei distribution of BMSCs on the hydrogel surface (scale bar, 40 μm). (**F**) Nuclei distribution of HUVECs on the hydrogel surface (scale bar, 40 μm). (**G**) XPS measurement spectra of SA and dopamine-SA. (**H**) Schematic diagram of changing hydrogel stiffness by changing the Ca^{2+} molar concentration. (**I**) Images and initial elastic modulus of hydrogels in different Ca^{2+} molar concentration groups (scale bar, 1 cm). (**J**) Scanning electron microscope images of different SA hydrogels (scale bar, 100 μm). (**K**) Pore diameter from scanning electron microscope image. (**L**) Images of SA-MSNs@CM-Stiff under different external mechanical forces such as bending and stretching (scale bar, 1 cm). (**M**) Images of shapes prepared using SA-MSNs@CM-Stiff (scale bar, 1 cm). $n = 3$ for each group. Error bars denote means $\pm$ SEM; *$P < 0.05$, **$P < 0.01$, and ***$P < 0.001$.
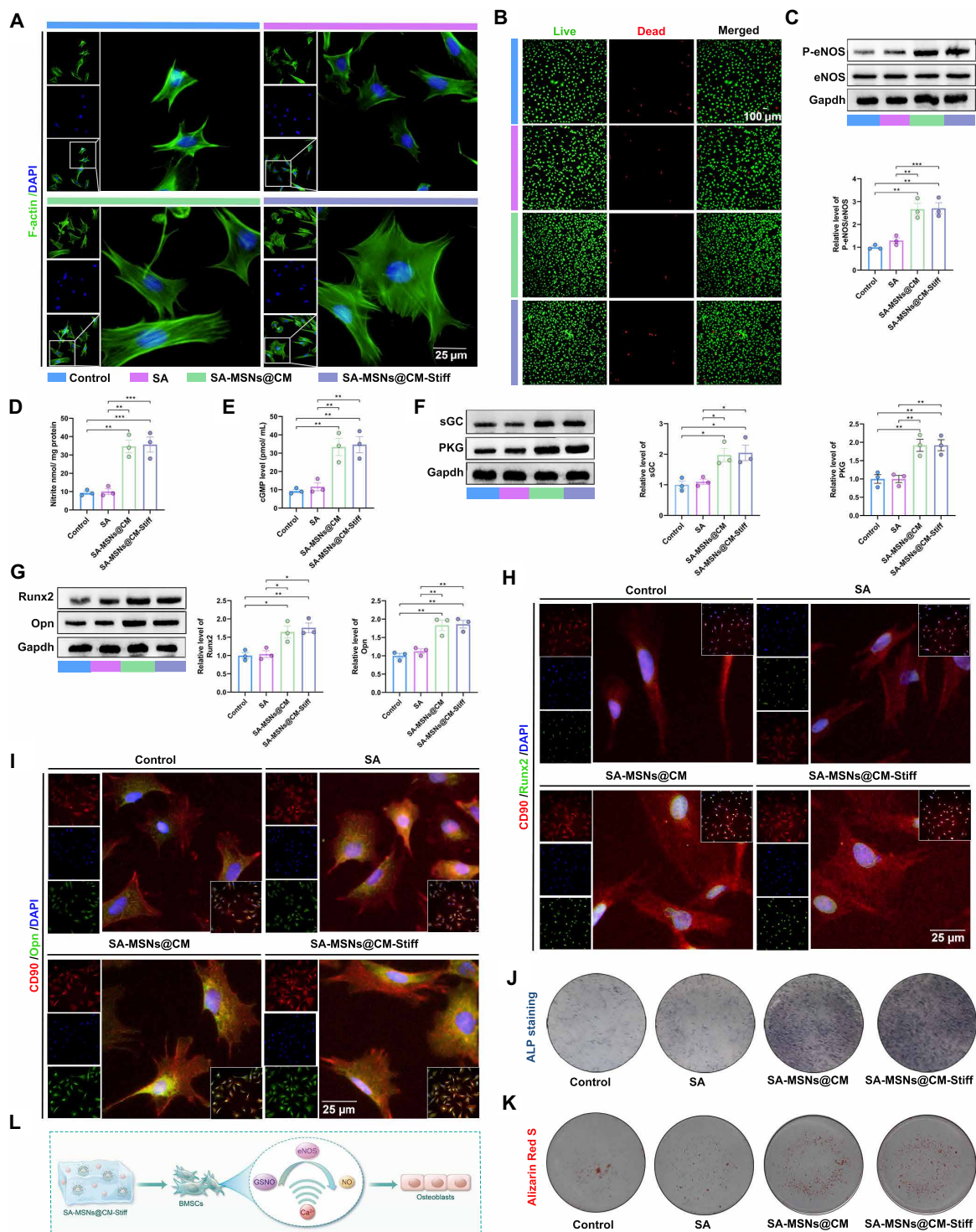
Fig. 4. SA-MSNs@CM-Stiff promotes osteogenesis by activating the NO/cGMP pathway in vitro. (**A**) Immunofluorescence staining of F-actin in BMSCs cultured with hydrogels for 7 days (scale bar, 25 μm). (**B**) Live/dead assay of BMSCs cultured with hydrogels for 3 days (scale bar, 100 μm). Live cells appear green, and dead cells appear red. (**C**) Western blots analysis of P-eNOS and eNOS levels in BMSCs cultured with hydrogels for 7 days. (**D**) NO generation in BMSCs cultured with hydrogels for 7 days indicated by nitrite levels. (**E**) cGMP expression in BMSCs cultured with hydrogels for 7 days. (**F**) Western blots analysis of sGC and PKG levels in BMSCs cultured with hydrogels for 7 days. (**G**) Western blots analysis of Runx2 and Opn levels in BMSCs cultured with hydrogels for 7 days. (**H**) Representative of immunofluorescence staining of CD90 and Runx2 in BMSCs cultured with hydrogels for 7 days (scale bar, 25 μm). (**I**) Representative of immunofluorescence staining of CD90 and Opn in BMSCs cultured with hydrogels for 7 days (scale bar, 25 μm). (**J**) The ALP staining of BMSCs cultured with hydrogels for 7 days. (**K**) Alizarin Red S staining of BMSCs cultured with hydrogels for 7 days. (**L**) Schematic diagram of SA-MSNs@CM-Stiff activating NO/cGMP pathway to promote BMSC osteogenesis. $n = 3$ for each group. Error bars denote means $\pm$ SEM; *$P < 0.05$, **$P < 0.01$, and ***$P < 0.001$.
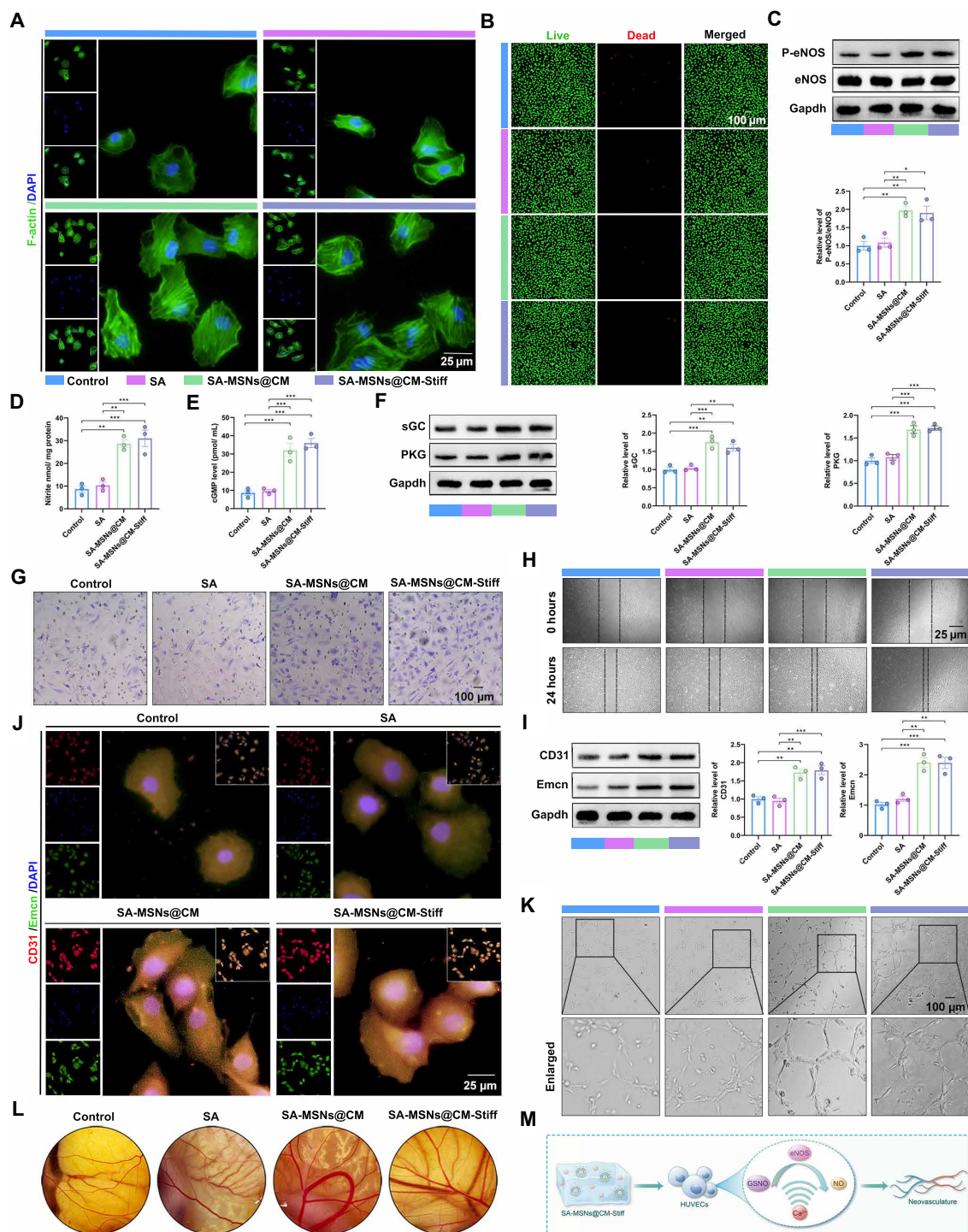
Fig. 5. SA-MSNs@CM-Stiff promotes migration and angiogenesis by activating the NO/cGMP pathway in vitro. (**A**) Immunofluorescence staining of F-actin in HUVECs cultured with hydrogels for 3 days (scale bar, 25 μm). (**B**) Live/dead assay of HUVECs cultured with hydrogels for 3 days (scale bar, 100 μm). Live cells appear green, and dead cells appear red. (**C**) Western blotting analysis of P-eNOS and eNOS levels in HUVECs cultured with hydrogels for 3 days. (**D**) NO generation in HUVECs cultured with hydrogels for 3 days, as indicated by nitrite levels. (**E**) cGMP expression in HUVECs cultured with hydrogels for 3 days. (**F**) Western blotting analysis of sGC and PKG levels in HUVECs cultured with hydrogels for 3 days. (**G**) Transwell was used to evaluate the effect of hydrogels on the migration capacity of HUVECs. (**H**) Scratch experiments were used to evaluate the effect of the hydrogels on the migration ability of HUVECs. (**I**) Western blotting analysis of CD31 and Emcn levels in HUVECs cultured with hydrogels for 3 days. (**J**) Representative immunofluorescence staining of CD31 and Emcn in HUVECs cultured with hydrogels for 3 days (scale bar, 25 μm). (**K**) Tubule formation experiments were used to evaluate the effect of hydrogels on the angiogenesis of HUVECs (scale bar, 100 μm). (**L**) Chick CAM was used to evaluate the effect of hydrogels on the angiogenesis. (**M**) Schematic diagram of SA-MSNs@CM-Stiff activating NO/cGMP pathway to promote HUVECs angiogenesis. $n = 3$ for each group. Error bars denote means ± SEM; *$P < 0.05$, **$P < 0.01$, and ***$P < 0.001$.

coculture (Fig. 5C). Similarly, NO levels increased significantly in the SA-MSNs@CM and SA-MSNs@CM-Stiff groups (Fig. 5D). Moreover, a significant increase in downstream signaling molecules, such as cGMP, sGC, and PKG, was observed in the SA-MSNs@CM and SA-MSNs@CM-Stiff groups (Fig. 5, E and F). We then examined the effect of hydrogels on migration. Under the same conditions, there was a significant increase in the number of cells passing through the Transwell chamber in the SA-MSNs@CM and SA-MSNs@CM-Stiff groups (Fig. 5G). After 24 hours, HUVECs in the SA-MSNs@CM and SA-MSNs@CM-Stiff groups demonstrated significant healing through migration (Fig. 5H). Last, we evaluated the effects of the different hydrogels on angiogenesis. Western blotting analysis revealed that CD31 and Emcn were significantly up-regulated in the SA-MSNs@CM and SA-MSNs@CM-Stiff groups (Fig. 5I). The results of the immunofluorescence experiments were comparable (Fig. 5J). Tubular structures were observed in HUVECs from the SA-MSNs@CM and SA-MSNs@CM-Stiff groups after 6 hours in the tubule formation experiment (Fig. 5K). A chicken chorioallantoic membrane (CAM) test was performed to evaluate the angiogenic properties of the hydrogels in vivo (30). The results indicated that more blood vessels were formed in the SA-MSNs@CM and SA-MSNs@CM-Stiff groups (Fig. 5L). These findings revealed that SA-MSNs@CM and SA-MSNs@CM-Stiff promoted the migration and angiogenesis of HUVECs (Fig. 5M).

SA-MSNs@CM-Stiff promotes migration and paracrine function of BMSCs in 3D condition

To better simulate the in vivo situation, BMSCs were cultured under 3D conditions. Calcein-AM/PI staining demonstrated that BMSCs exhibited a high survival rate in all the groups (Fig. 6A). A notable increase in the number of cells that passed through the Transwell chamber was observed in the SA-MSNs@CM-Stiff group (Fig. 6B). Staining the cytoskeleton with phalloidin indicated that the hydrogel affected the cell extension state, and the cell morphology was not different among the matrix stiffness groups (Fig. 6C). A previous study confirmed that the paracrine effects of BMSCs can be affected by hydrogel stiffness (25). Next, we determined whether different hydrogels affect the expression of paracrine factors in BMSCs. The SA-MSNs@CM-Stiff group expressed higher human growth factor (HGF), prostaglandin E2 (PEG2), stromal cell derived factor 1 (SDF-1), and vascular endothelial growth factor–A (VEGF-A) levels than the other groups (Fig. 6D). On the basis of the above results, SA-MSNs@CM-Stiff promotes the paracrine effect of BMSCs (Fig. 6E).

SA-MSNs@CM-Stiff regulates macrophage polarization by promoting BMSCs paracrine in 3D condition

The following experiments were conducted to investigate the paracrine effects of BMSCs on macrophage polarization. To determine the effects of BMSCs paracrine on macrophage polarization, we treated various groups of macrophages with a BMSCs-conditioned medium (Fig. 7A). According to flow cytometry analysis, SA-MSNs@CM-Stiff exhibited significantly fewer CD86+ macrophages (Fig. 7B). Moreover, SA-MSNs@CM-Stiff exhibited a significantly higher proportion of CD206+ macrophages (Fig. 7C). A significant decrease in CD86 expression was observed in the SA-MSNs@CM-Stiff group compared to the other groups (Fig. 7D). Contrary to this, SA-MSNs@CM-Stiff expressed notably more CD206 (Fig. 7E). Similar results were obtained in the Western blotting experiments (Fig. 7F). Correspondingly, polarized macrophages significantly up-regulated the secretion of the
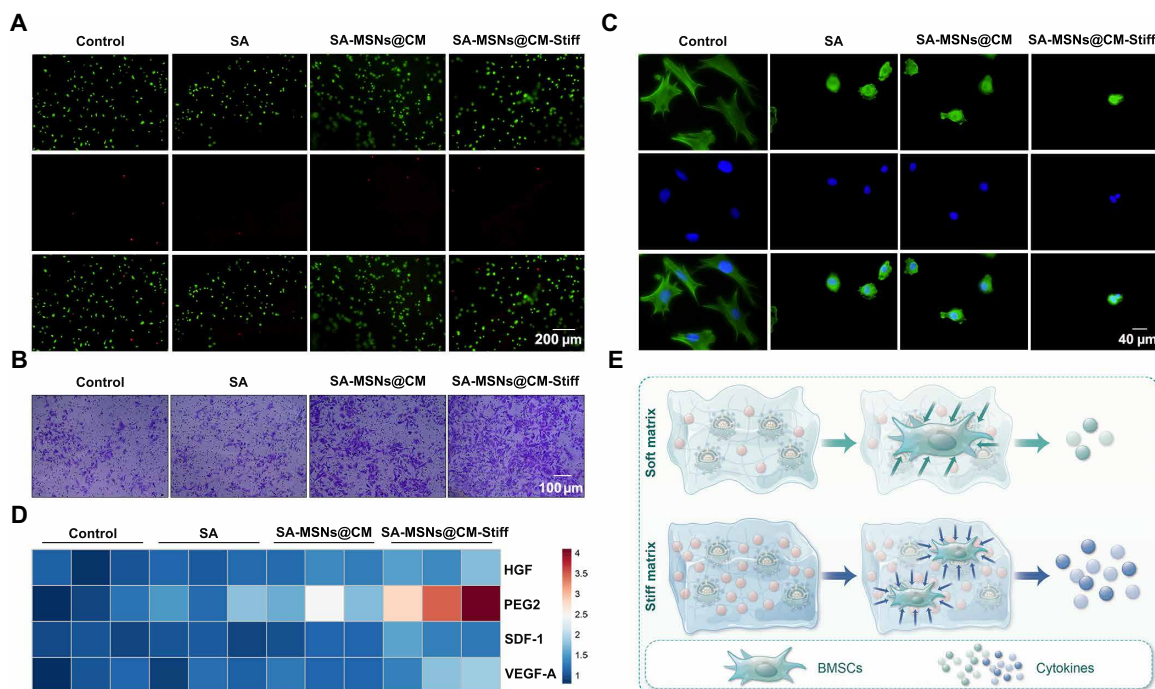

Fig. 6. SA-MSNs@CM-Stiff promotes migration and paracrine function of BMSCs under 3D conditions. (**A**) Live/dead assay of BMSCs cultured with hydrogels under 3D conditions for 3 days (scale bar, 200 μm). Live cells appear green, and dead cells appear red. (**B**) The Transwell assay was used to evaluate the effect of hydrogels on the migration capacity of BMSCs cultured with hydrogels under 3D conditions for 3 days (scale bar, 100 μm). (**C**) Immunofluorescence staining of F-actin in BMSCs cultured with hydrogels under 3D conditions for 3 days (scale bar, 40 μm). (**D**) HGF, PEG2, SDF-1, and VEGF-A expression in BMSCs cultured with hydrogels under 3D conditions for 3 days. (**E**) Schematic diagram of SA-MSNs@CM-Stiff promotes migration and paracrine function of BMSCs under 3D conditions. $n = 3$ for each group. Error bars denote means ± SEM; *$P < 0.05$, **$P < 0.01$, and ***$P < 0.001$.

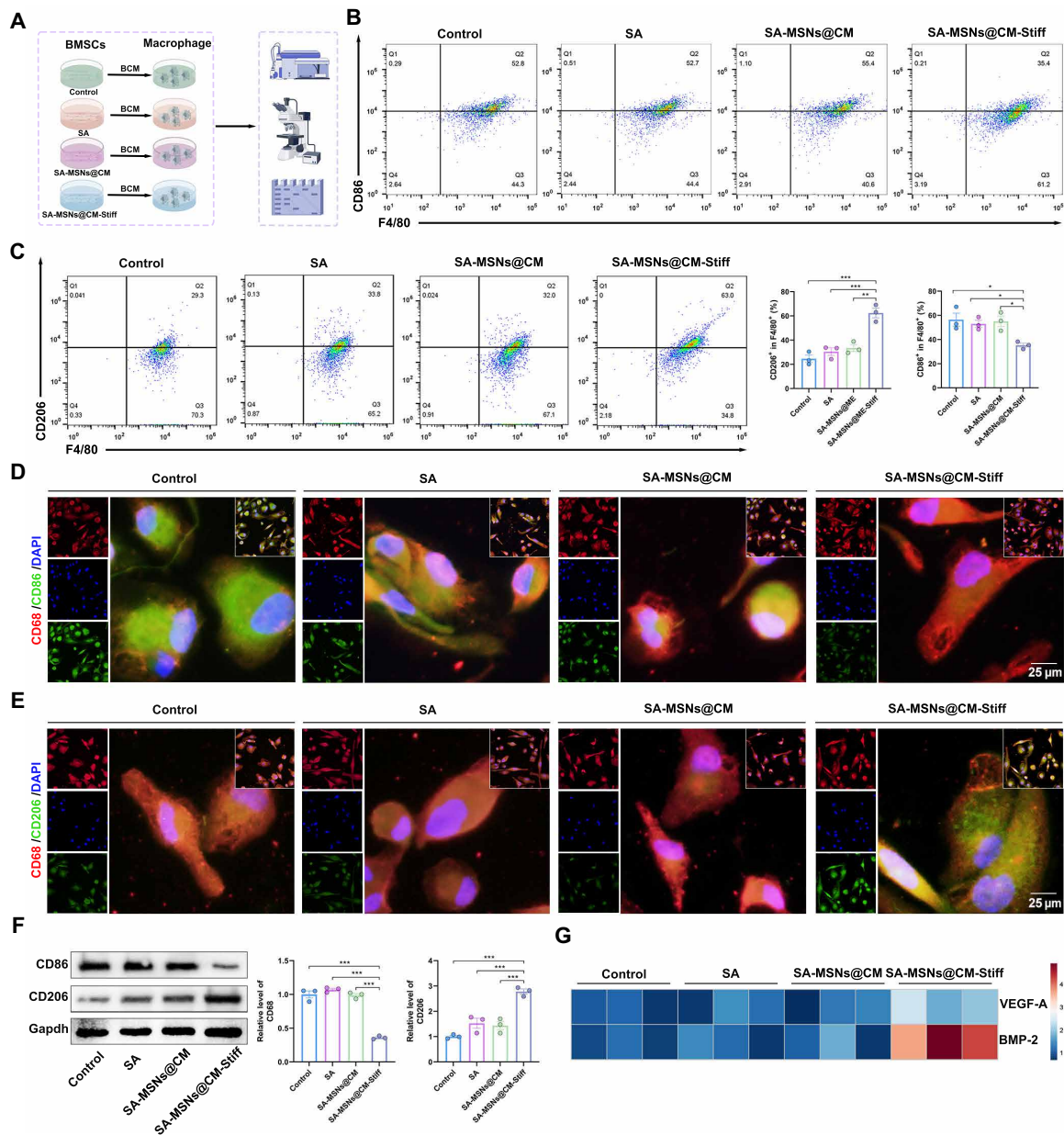**Fig. 7. SA-MSNs@CM-Stiff regulates macrophage polarization by promoting BMSCs paracrine under 3D conditions.** (**A**) Protocol of in vitro experiments for detecting macrophage polarization regulated by BMSCs paracrine (by Figdraw). BMSCs were cultured with hydrogels for 3 days. After removal of the supernatant, cells were cultured in Dulbecco's modified Eagle's medium (DMEM)/F12 for 3 days, and the supernatant was collected as THP-1 conditioned medium for 2 days. BCM, BMSCs-conditioned medium. (**B**) Flow cytometric analysis of the expression levels of M1 macrophages (F4/80/ CD86$^+$). (**C**) Flow cytometric analysis of the expression levels of M2 macrophages (F4/80/ CD206$^+$). (**D**) Representative immunofluorescence staining for CD68 and CD86 in THP-1 cells (scale bar, 25 μm). (**E**) Representative immunofluorescence staining for CD68 and CD206 in THP-1 cells (scale bar, 25 μm). (**F**) Western blot analysis of CD86 and CD206 levels in macrophages. (**G**) VEGF-A and BMP-2 expression in macrophages. $n = 3$ for each group. Error bars denote means ± SEM; *$P < 0.05$, **$P < 0.01$, and ***$P < 0.001$.

angiogenic factor VEGF-A and osteogenesis-related molecule bone morphogenetic protein–2 (BMP-2) (Fig. 7G). On the basis of these results, BMSCs paracrine might regulate macrophage polarization.

SA-MSNs@CM-Stiff induces BMSCs recruitment and promotes osseointegration in vivo

Because of the complex local microenvironment, patients with osteoporosis experience a slower postfracture healing rate due to the fact that osteoblast-mediated bone formation is significantly lower than osteoclast-mediated bone resorption (*31*). SA-MSNs@CM-Stiff can promote osteogenesis in vitro, but its potential in vivo effects remain unknown. Consequently, we used a rat model of osteoporotic bone defects to evaluate the ability of each hydrogel to promote bone reconstruction (Fig. 8A). No biological toxicity was observed in vitro for either hydrogel (fig. S4, A and B). Although new bone formation occurred in all groups of rats implanted, it was

most pronounced in the group of rats injected with SA-MSNs@CM-Stiff (Fig. 8, B and D). After 8 weeks of treatment, the SA-MSNs@CM-Stiff group exhibited a 1.78-fold increase in bone mineral density and a 2.54-fold increase in bone tissue volume/total tissue volume compared to the control group (Fig. 8C). In addition, trabecular thickness and trabecular number in the SA-MSNs@CM-Stiff group significantly increased (Fig. 8C). H&E and Masson staining also demonstrated the excellent bone-promoting ability of SA-MSNs@CM-Stiff (Fig. 8, E and F).

We performed further investigation of the role of hydrogels in osteogenesis-angiogenesis coupling using immunofluorescence staining. These results indicated that SA-MSNs@CM-Stiff exhibited a notably greater number of highly positive CD31 and Emcn cells than the other groups (Fig. 8G and fig. S5A). The blood vessels in bones are functionally specialized. Endothelial cells in H-type blood vessels express high levels of CD31 and Emcn, which provide angiokinesis to act on BMSCs and couple angiogenesis and osteogenesis (7). Furthermore, double immunostaining of Runx2 and Opn with cell markers (CD90) confirmed the increased expression of Runx2 and Opn in BMSCs of the SA-MSNs@CM-Stiff group (Fig. 8, H and I, and fig. S5, B and C). In addition, the SA-MSNs@CM-Stiff group exhibited a significantly lower expression of inducible nitric oxide synthase (iNOS) in macrophages than the other groups in vivo (fig. S6). Conversely, a notable increase in CD206 expression was observed (fig. S6). The above results confirm that SA-MSNs@CM-Stiff can promote the healing of osteoporotic bone defects by promoting osteogenesis and vascular coupling.

DISCUSSION

Approximately 9 million osteoporotic fractures per year occur globally (32), with osteoporotic fractures every 4 s, resulting in various bone defects. Consequently, there is an urgent need for materials with good biocompatibility and the ability to promote osteogenesis. Previous studies have primarily focused on normal bone defects (6, 33) rather than osteoporotic bone defects (5). However, osteoporotic bone defects are more difficult to heal than normal ones. This study demonstrated that BMSCs derived from osteoporotic rats had a significantly reduced osteogenic capacity. Therefore, it is critical to regulate the osteogenic ability of BMSCs to promote osteoporotic bone healing. We developed a biomimetic nanomaterial in this study to promote osteogenesis and angiogenesis and modulate immunology.

NO is a key gas transmitter that maintains homeostasis and vascular patency (34). NO can inhibit platelet aggregation (35), promote vascular endothelium regeneration (12), and prevent vascular calcification (36). In the present study, we developed biomimetic nanoparticles that deliver GSNO and used SA to release calcium ions to promote NO production and synergize downstream signaling pathways. These findings indicate that SA-MSNs@CM-Stiff promotes vascular endothelial migration and angiogenesis. Yang et al. (33) developed materials that deliver L-arginine that can promote angiogenesis. Unfortunately, the effects of the material on vascular endothelial migration were not investigated. Vascular endothelial cells at the defect site migrated from the surrounding area. Previous studies have established a correlation among the NO/cGMP pathway, osteogenesis, and angiogenesis (6, 37). Similar findings were observed in BMSCs from osteoporotic rats in this study. We demonstrated that NO/cGMP activation is useful in osteoporotic rat–derived BMSCs. However, direct administration of GSNO is hindered by low cellular internalization and rapid phagocytosis by macrophages.

In addition, NO production can regulate macrophages from the M2 phenotype, which promotes tissue repair, to the M1 phenotype, which promotes tissue inflammation (38). Ideally, a drug delivery system should effectively regulate the loading process and release rate to precisely target the desired tissues or cells (13, 39).

In this study, we developed a biomimetic hydrogel for the targeted delivery of GSNO to BMSCs and HUVECs. To circumvent macrophage phagocytosis, we modified the CD47 molecule on MSNs, an antiphagocytic signal (40). BMSCs also play an important role in bone repair (6). A short peptide sequence, SKPPGTSS, has been reported to promote mesenchymal stem cell homing by mimicking the structure of BMHP (22). Our findings indicate that SA-MSNs@CM-Stiff facilitates BMSC homing. However, it is difficult for these nanoparticles to remain in the defect sites for a long time.

Recently, injectable hydrogels have gained notable attention owing to their potential applications in bone regeneration (5). The hydrogels retained the biomimetic nanoparticles at the defect site. These hydrogels consist of only colloidal particles. Various particles can be used as colloidal building blocks, suitable for functionalization with drugs or biomolecules (3, 33). Because of the reversibility of the interparticle bonds, these composite colloidal gels are capable of self-healing (41). Furthermore, the dynamics and adaptability of the hydrogel network can provide a favorable microenvironment for tissue growth and cell viability (42, 43), which may lead to improved bone regeneration. SA can chelate divalent cations to produce hydrogels (44). In this study, we chelated SA with calcium ions to form hydrogels that provide a scaffold for cells. However, SA lacks cell adhesion sites (21). In this study, the SA backbone molecules were covalently bound to dopamine. These findings demonstrated that the modified hydrogel exhibited better biocompatibility. Previous studies have indicated that matrix stiffness may enhance the paracrine function of BMSCs (44, 45). A linear correlation was observed between the stiffness of SA hydrogels and the dose of divalent cation (25). We used Ca^{2+} in this study to increase matrix stiffness. The results revealed that SA-MSNs@CM-Stiff promoted the paracrine effects of BMSCs, which subsequently regulated macrophage polarization.

Together, we demonstrated that osteoporotic bone defects can be successfully regenerated using bioactive composite colloidal gels composed of dopamine-functionalized SA and MSNs with GSNO. We modified SA with dopamine to enhance biocompatibility and chelated with calcium ions to improve stiffness. A sustained supply of GSNO and Ca^{2+} from SA-MSNs@CM-Stiff activates the NO/cGMP signaling pathway, followed by well-coordinated osteogenic-angiogenesis coupling effects during bone repair. Nanomaterials have been functionalized with CMs to improve targeting and biocompatibility. In this study, the biomimetic nanomaterial was designed to incorporate the molecular mechanisms of osteogenesis and angiogenesis to further improve the microenvironment for bone defect healing by modulating the matrix stiffness to have immunomodulatory functions. It is anticipated that our SA-MSNs@CM-Stiff will be a valuable tool for mitigating the problem of delayed or even nonhealing of osteoporotic bone defects.

MATERIALS AND METHODS
Establishment of osteoporosis model
Nine-month-old rats were ovariectomized to establish an osteoporosis model. Intraperitoneal injections of 1% pentobarbital (0.1 ml/100 g) were administered to anesthetize the rats. Under complete anesthesia, the surgery was performed in the prone position. Previously
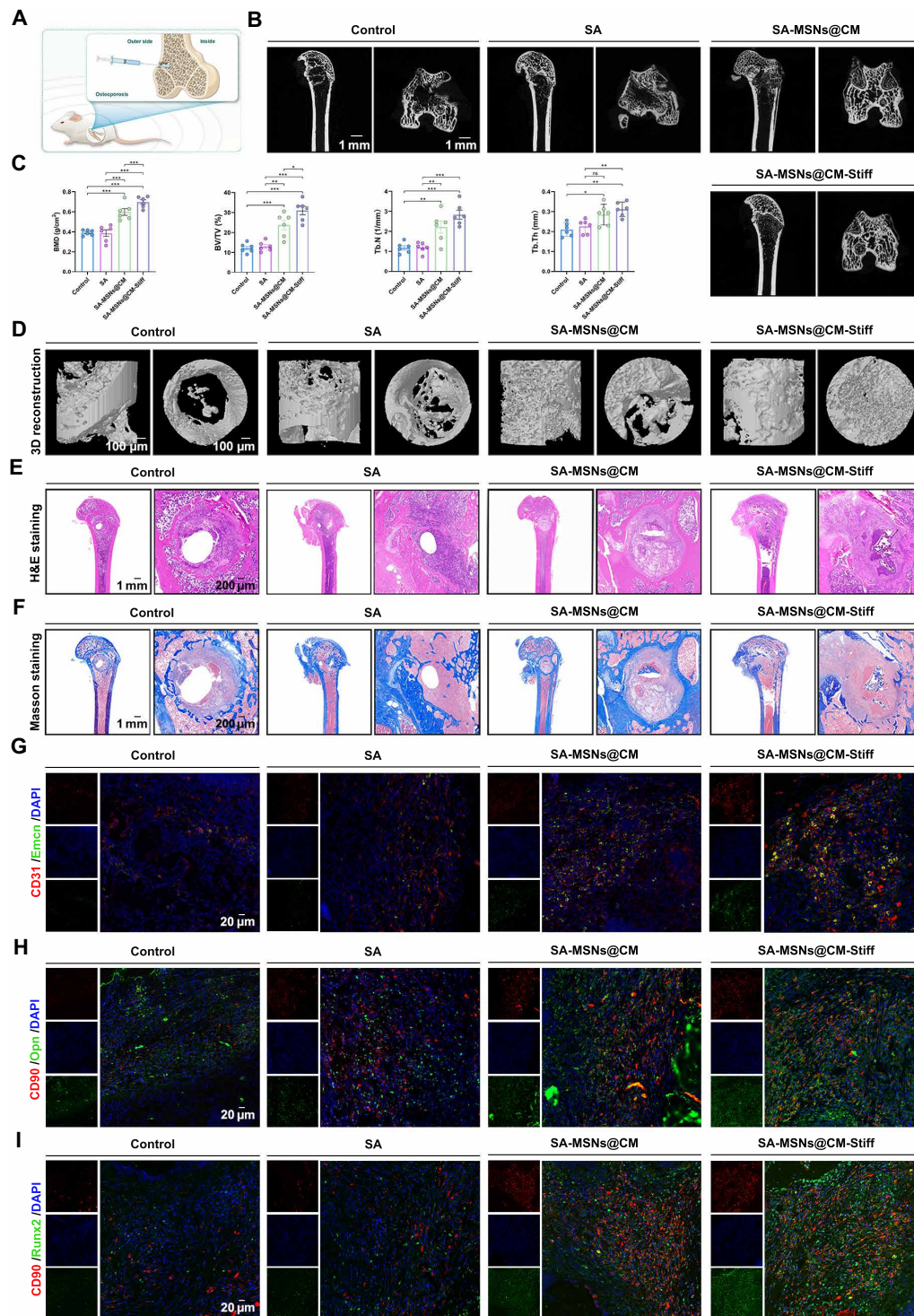
Fig. 8. SA-MSNs@CM-Stiff induces BMSCs recruitment and promotes osseointegration in vivo. (**A**) Schematic illustration of hydrogel implantation. (**B**) Typical micro-CT images of the distal femur of rats with osteoporotic bone defects at 8 weeks. (**C**) Quantitative analysis of bone density, volume, and other parameters. BMD, bone mineral density. (**D**) 3D reconstruction results. (**E**) H&E staining images of different groups (scale bar, 1 mm and 200 μm). (**F**) Masson staining images of different groups (scale bar, 1 mm and 200 μm). (**G**) Representative immunofluorescence staining of CD31 and Emcn in the femoral condyle of an osteoporotic rat 8 weeks after hydrogel implantation (scale bar, 20 μm). (**H**) Representative immunofluorescence staining of CD90 and Opn in the femoral condyle of an osteoporotic rat 8 weeks after hydrogel implantation (scale bar, 20 μm). (**I**) Representative immunofluorescence staining of CD90 and Runx2 in the femoral condyle of an osteoporotic rat 8 weeks after hydrogel implantation (scale bar, 20 μm). $n = 6$ for each group. Error bars denote means ± SEM; *$P < 0.05$, **$P < 0.01$, and ***$P < 0.001$.

described ovariectomies were performed in these rats (*3*). After 3 months, the distal femurs of the rats were collected for micro-CT scans to assess the efficacy of the osteoporosis rat model. All experimental procedures were approved by the Ethics Committee and Institutional Review Board of the Fourth Military Medical University (Air Force Military Medical University, IACUC-20230095).

Histological evaluation
The fixed tissue was gently shaken and decalcified with a 10% EDTA solution for 4 weeks. Conventional paraffin embedding after decalcification was performed, and all specimens were kept in the same position as possible. Sections of 4-μm thickness were cut from them. H&E and Masson staining were performed with the H&E dye solution set and Masson dye solution set (Servicebio, China) for histological evaluation.

Cell culture
According to a previous study (*29*), BMSCs were isolated from the femurs of young (6-month-old), middle-aged (12-month-old), and ovariectomized (12-month-old) rats. Dulbecco's modified Eagle's medium (DMEM)/F12–based culture medium with penicillin/streptomycin and fetal bovine serum (FBS) (InCellGene, USA) was used to culture rat primary BMSCs. HUVECs and THP-1 cells were cultured in endothelial cell medium (Sciencell, USA) and RPMI 1640 medium with FBS and penicillin/streptomycin, respectively. Standard protocols were used to differentiate THP-1 cells into M0 (*46*).

Differentiation potential of BMSCs
Osteogenic induction of BMSCs was completed using a mesenchymal stem cell osteogenic differentiation induction kit (iCell-MSCYD-002, iCell Bioscience). Chondrogenic induction was performed using a mesenchymal stem cell chondrogenic differentiation induction kit (iCell-MSCYD-003, iCell Bioscience). Furthermore, a mesenchymal stem cell osteogenic differentiation induction kit (iCell-MSCYD-004, iCell Bioscience) was used to induce the adipogenic differentiation of BMSCs. We followed the manufacturer's instructions for these procedures (iCell Bioscience).

β-Galactosidase staining
Cellular senescence–associated-galactosidase activity (SA-β-gal) was assessed according to the manufacturer's instructions (Solarbio, China). Cells were suspended in six-well plates at a density of 2×10^5 cells in a DMEM/F12 medium. After washing the cells with phosphate-buffered saline (PBS), they were incubated for 12 hours at 37°C in staining solution. Last, the cells were incubated for 1 min at 37°C in hematoxylin dye solution.

Flow cytometry
Flow cytometry was used to characterize the extracted BMSCs (P3) to detect the expression profile of surface molecules, such as CD29, CD34, CD44, CD45, CD73, and CD90. Different groups of macrophages were detected using phycoerythrin (PE) anti-CD86 (eBioscience, USA), PE anti-CD206 (eBioscience, USA), and allophycocyanin (APC) anti-F4/80 (Biolegend Co., USA). The binding buffer was prepared to resuspend the cells after washing with PBS. A 15-min staining procedure was conducted at 4°C using antibodies. FlowJo software (version 10.6.2) was used to analyze the samples after they were detected using a flow cytometer (BD Biosciences).

Western blotting
Radioimmunoprecipitation assay lysis buffer containing protease and phosphatase inhibitors was used to extract proteins from human BMSCs, HUVECs, and THP-1 cells. We separated 20 μg of protein per lane using 10 to 12% SDS–polyacrylamide gel electrophoresis and transferred the samples to polyvinylidene difluoride membranes (Millipore). After blocking with 5% nonfat milk, primary antibodies were incubated overnight at 4°C. Antibody information is in the table S1. Next, anti-mouse or anti-rabbit secondary antibodies (1:5000; AS003, AS014, ABclonal) were added to the membranes. Enhanced chemiluminesence reagents (ABclonal, China) were used to incubate the membranes.

Immunofluorescence
As described previously (*47*), immunohistochemistry was used to stain the tissue. The bone tissues were first decalcified. Paraffin-embedded bone tissues were cut into 4-mm-thick sections. The sections were deparaffinized, rehydrated, and blocked with 5% bovine serum albumin (BSA; Gibco) at room temperature for 1 hour. Primary BMSCs, HUVECs, and THP-1 cells were washed thrice with PBS, followed by blocking with 5% BSA. Antibody information is in the table S2. Sections were incubated overnight with specific antibodies at 4°C. Subsequently, the corresponding secondary antibodies were incubated for 50 min at room temperature in the dark. The nuclei were labeled with 4′,6-diamidino-2-phenylindole (DAPI) (1:1000; Invitrogen).

Staining of ALP
BMSCs were treated and induced for 10 days. After washing with PBS, cells were fixed with 4% paraformaldehyde at room temperature for 30 min. Following two washes in PBS, BMSCs were incubated for 6 hours in ALP staining buffer (Beyotime Institute of Biotechnology, China).

Synthesis of MSNs-GSNO@CM
The MSNs were prepared according to a previous study (*48*). The exact details have been described in our previous study (*17*). To encapsulate GSNO, MSNs (10 mg) were added to 3 ml of the GSNO solution (1 mg/ml) and stirred for 6 hours in an ice bath. MSNs-GSNO were separated from the unincorporated GSNO using centrifugation.

As illustrated in Fig. 1, the MSNs-GSNO were cloaked in the CMs (MSNs-GSNO@CM): BMSC and HUVEC CMs and MSNs-GSNO were mixed and extruded through a 220-nm polycarbonate membrane to form MSNs-GSNO@CM.

Characterization of the MSNs and MSNs@CM
The MSNs and MSNs@CM were analyzed by TEM (JEM-1230, Japan). Zetasizer Nano-ZS dynamic light scattering (DLS) was used to determine the hydrodynamic size of nanoparticle aggregates. DLS was used to evaluate the zeta potential of the MSNs and MSNs@CM (Beckman Coulter Instruments, USA).

Synthesis of SA-dopamine
After removing 2.132 g of MES from the reagent bottle and dissolving it in 100 ml of deionized water, 1.75 g of NaCl was added, followed by 0.1 M NaOH to adjust the pH of the solution to 6.5. SA (1.08 g) was added to 60 ml of MES buffer and fully dissolved by ultrasonication and agitation. The carboxyl group was activated by

adding 19 mg of EDC●HCl, and 11.5 mg of *N*-hydroxysuccinimide was added to the solution and stirred for 2 hours at 500 rpm. Then, 15.3 mg of dopamine was added. After 24 hours of reaction at room temperature, dialysis bags with a molecular weight of 600 MW were used to perform dialysis in deionized water for 3 days. After 3 days, the dialysis products were filtered, sterilized, freeze dried, and stored for later use.

Synthesis of SA hydrogels
BMHP (SKPPGTSS-NH2) (purity: 96.85%) was synthesized and purified by ChinaPeptides Co., Ltd. (Shanghai, China). The purity and identity of the peptides were determined by high-performance liquid chromatography analysis and electrospray ionization mass spectrometry (fig. S7, A and B). SA hydrogels with five stiffness values were obtained by mixing functionalized SA and different concentrations of calcium chloride $CaCl_2$ solution (20, 30, 40, 50, or 60 mM $CaCl_2$). The appropriate hardness of hydrogels was selected. Then, functionalized SA, MSNs@CM, 1% w/v BMHP, and $CaCl_2$ was mixed to obtain SA-MSNs@CM (20 mM $CaCl_2$) and SA-MSNs@CM-Stiff (50 mM $CaCl_2$).

Characterization of the SA, SA-MSNs@CM, and SA-MSNs@CM-Stiff
XPS (Thermo Fisher Scientific K-Alpha, USA) was used to confirm the successful grafting of dopamine onto SA. The cell nuclei were stained with DAPI to observe the adhesion of the hydrogel to the cells. Compression tests were performed to determine the initial elastic modulus of alginate hydrogels. Briefly, the hydrogel disk was placed on a CMT6103 (MTS, USA) platform, and a compression test model was used. A previous study described this method in detail (*25*). The cut and freeze-dried samples were observed using the scanning electron microscope (ZEISS Sigma 300, Germany). A random set of scanning electron microscope images was recorded, and the pore size of each sample was measured using the ImageJ software.

Calcein-AM/PI staining
By staining BMSCs and HUVECs with calcein-AM and PI, we assessed the viability of the cells after 3 days of culture. The cells were incubated in the dark for 20 min at 37°C in a 5% CO_2 cell culture incubator after adding calcein-AM/PI reagent to each medium. Last, the cells were observed under a microscope after washing with PBS.

The concentration of NO
NO concentration was determined using the Griess method. First, the Griess Reagents I and II were removed and returned to room temperature. The standard was diluted with a cell medium. The standard and sample were then added to a labeled 96-well plate at 50 µl per well. Griess Reagent I (50 µl) and Griess Reagent II (50 µl) were added. Last, the absorbance of each well was measured at 540-nm wavelength. The NO concentration was calculated on the basis of a standard product curve.

Enzyme-linked immunosorbent assay
The supernatants of the cell culture were collected by centrifuging at 2000 to 3000 rpm for 20 min after transferring them into sterile tubes. The supernatants were analyzed using enzyme-linked immunosorbent assay kits (E-EL-0083, E-EL-R0496, E-EL-0034, E-EL-R3027, E-EL-R2603, and E-EL-H0011; Elabscience) to measure cGMP, HGF, PGE2, SDF-1, VEGF-A, and BMP-2 levels. In accordance with the manufacturer's instructions, all assays were performed (Elabscience, China).

Migration and invasion assay
An assay for wound healing was used to measure cell migration. HUVECs were seeded in a six-well plate at a density of 5×10^5 cells per well. After 12 hours, a scratch was made using a 200-µl pipette tip, and a serum-free medium was used. A 0-hour image was taken, the plates were returned to the incubator for 24 hours, and a 24-hour image was obtained.

Cell invasion was measured using a Transwell assay. Transwell inserts (2×10^4 cells per well) with micropore filters (Corning Costar, MA, USA) were seeded with the HUVECs. A lower chamber medium containing 10% FBS was added. The effect of hydrogel stiffness on the migration of BMSCs was evaluated using 3D cultures. First, BMSCs at a density of 3×10^4/ml were mixed with different groups of hydrogels and inoculated into the upper layer of Transwell cells. Subsequently, the medium without FBS was added to the upper layer. A complete medium was added to the lower layer. Last, cells were incubated in an incubator. A final fixation and staining procedure was performed after the upper side cells were removed after 24 hours. Optical microscopy was used to observe the invading cells.

Tubule formation assays of HUVECs
A tubule formation assay was performed using Matrigel (No.354234; Corning) to measure the vascularization ability. HUVECs were cocultured with hydrogels for 48 hours, and then 2×10^5 cells were added to each well of a 24-well plate coated with Matrigel. An inverted microscope was used to capture images after 6 hours.

Vascularization in a CAM model
Embryos were developed from fertilized chicken eggs and incubated in a humidified incubator at 37°C for 7 days. The air chamber was cut at the corresponding shell position, and a small window was opened (1 cm^2). The hydrogels were placed on the CAM surface. The parafilm shell was resealed. Fertilized eggs were then returned to the incubator for an additional 7 days. Last, the CAM complexes were photographed.

Evaluation of bone repair in vivo
The effects of biomimetic hydrogels on bone reconstruction were evaluated using bone-defect models. Osteoporosis was confirmed 3 months later using micro-CT. A bone defect (4×5 mm^2) was produced by inserting a 3.5-mm electric drill into the lateral epicondyle of the femur. The left or right femur of each animal was implanted with SA colloid. Then, calcium chloride was injected into the corresponding site for ion cross-linking. After 8 weeks, the rats were euthanized via an anesthetic overdose. The femoral condyle was dissected, adherent tissue removed, and fixed in neutral-buffered formaldehyde for 48 hours for further analysis.

Statistical analysis
GraphPad Prism (version 9.0) was used for statistical analyses. Data from at least three independent experiments are presented as means ± SEM. Two independent groups were analyzed using an unpaired two-tailed Student's *t* test, whereas multiple groups were analyzed using a one-way analysis of variance followed by Tukey's post hoc tests for multiple comparisons. The significance of the study was defined as a two-sided *P* value <0.05.

Supplementary Materials

This PDF file includes:
Figs. S1 to S7
Tables S1 and S2

REFERENCES AND NOTES

1. J. E. Compston, M. R. McClung, W. D. Leslie, Osteoporosis. *Lancet* **393**, 364–376 (2019).
2. D. M. Black, C. J. Rosen, Clinical practice. Postmenopausal osteoporosis. *N. Engl. J. Med.* **374**, 254–262 (2016).
3. Z. Zhao, G. Li, H. Ruan, K. Chen, Z. Cai, G. Lu, R. Li, L. Deng, M. Cai, W. Cui, Capturing magnesium ions via microfluidic hydrogel microspheres for promoting cancellous bone regeneration. *ACS Nano* **15**, 13041–13054 (2021).
4. H. C. Pape, A. Evans, P. Kobbe, Autologous bone graft: Properties and techniques. *J. Orthop. Trauma* **24**, S36–S40 (2010).
5. M. Diba, W. A. Camargo, M. Brindisi, K. Farbod, A. Klymov, S. Schmidt, M. J. Harrington, L. Draghi, A. R. Boccaccini, J. A. Jansen, J. J. J. P. van den Beucken, S. C. G. Leeuwenburgh, Composite colloidal gels made of bisphosphonate-functionalized gelatin and bioactive glass particles for regeneration of osteoporotic bone defects. *Adv. Funct. Mater.* **27**, 1703438 (2017).
6. T. Xu, Y. Yang, D. Suo, H. Bei, X. Xu, X. Zhao, Electrosprayed regeneration-enhancer-element microspheres power osteogenesis and angiogenesis coupling. *Small* **18**, e2200314 (2022).
7. A. P. Kusumbe, S. K. Ramasamy, R. H. Adams, Coupling of angiogenesis and osteogenesis by a specific vessel subtype in bone. *Nature* **507**, 323–328 (2014).
8. M. Yang, C. J. Li, X. Sun, Q. Guo, Y. Xiao, T. Su, M. L. Tu, H. Peng, Q. Lu, Q. Liu, H. B. He, T. J. Jiang, M. X. Lei, M. Wan, X. Cao, X. H. Luo, MiR-497~195 cluster regulates angiogenesis during coupling with osteogenesis by maintaining endothelial Notch and HIF-1α activity. *Nat. Commun.* **8**, 16003 (2017).
9. C. Bogdan, Nitric oxide synthase in innate and adaptive immunity: An update. *Trends Immunol.* **36**, 161–178 (2015).
10. J. Kim, B. C. Yung, W. J. Kim, X. Chen, Combination of nitric oxide and drug delivery systems: Tools for overcoming drug resistance in chemotherapy. *J. Control. Release* **263**, 223–230 (2017).
11. Y. Sung, P. Jin, L. Chu, F. Hsu, M. Wang, C. Chang, S. Chiou, J. Qiu, D. Gao, C. Lin, Y. Chen, Y. Hsu, J. Wang, F. Wang, P. Yu, A. Chiang, A. Wu, J. Ko, C. Lai, T. Lu, Y. Chen, Delivery of nitric oxide with a nanocarrier promotes tumour vessel normalization and potentiates anti-cancer therapies. *Nat. Nanotechnol.* **14**, 1160–1169 (2019).
12. F. Wang, K. Qin, K. Wang, H. Wang, Q. Liu, M. Qian, S. Chen, Y. Sun, J. Hou, Y. Wei, Y. Hu, Z. Li, Q. Xu, Q. Zhao, Nitric oxide improves regeneration and prevents calcification in bio-hybrid vascular grafts via regulation of vascular stem/progenitor cells. *Cell Rep.* **39**, 110981 (2022).
13. Z. Li, J. Barnes, A. Bosoy, J. Stoddart, J. Zink, Mesoporous silica nanoparticles in biomedical applications. *Chem. Soc. Rev.* **41**, 2590–2605 (2012).
14. C. Huang, T. Xie, Y. Liu, S. Yan, F. OuYang, H. Zhang, L. Lei, D. He, H. Wei, C. Yu, A sodium alginate-based multifunctional nanoplatform for synergistic chemo-immunotherapy of hepatocellular carcinoma. *Adv. Mater.* **35**, e2301352 (2023).
15. P. Mora-Raimundo, D. Lozano, M. Benito, F. Mulero, M. Manzano, M. Vallet-Regí, Osteoporosis remission and new bone formation with mesoporous silica nanoparticles. *Adv. Sci.* **8**, e2101107 (2021).
16. P. Mora-Raimundo, D. Lozano, M. Manzano, M. Vallet-Regí, Nanoparticles to knockdown osteoporosis-related gene and promote osteogenic marker expression for osteoporosis treatment. *ACS Nano* **13**, 5451–5464 (2019).
17. F. L. Wei, T. F. Wang, C. L. Wang, Z. P. Zhang, J. W. Zhao, W. Heng, Z. Tang, M. R. Du, X. D. Yan, X. X. Li, Z. Guo, J. X. Qian, C. P. Zhou, Cytoplasmic escape of mitochondrial DNA mediated by Mfn2 downregulation promotes microglial activation via cGas-Sting axis in spinal cord injury. *Adv. Sci.* **11**, e2305442 (2024).
18. J. Kretlow, S. Young, L. Klouda, M. Wong, A. Mikos, Injectable biomaterials for regenerating complex craniofacial tissues. *Adv. Mater.* **21**, 3368–3393 (2009).
19. Y. Luo, G. Li, L. Chen, F. Hong, Preparation and evaluation of bacterial nanocellulose/hyaluronic acid composite artificial cornea for application of corneal transplantation. *Biomacromolecules* **24**, 201–212 (2023).
20. L. Zhao, L. Pan, K. Zhang, S. Guo, W. Liu, Y. Wang, Y. Chen, X. Zhao, H. Chan, Generation of Janus alginate hydrogel particles with magnetic anisotropy for cell encapsulation. *Lab Chip* **9**, 2981–2986 (2009).
21. O. Chaudhuri, L. Gu, D. Klumpers, M. Darnell, S. Bencherif, J. Weaver, N. Huebsch, H. Lee, E. Lippens, G. Duda, D. Mooney, Hydrogels with tunable stress relaxation regulate stem cell fate and activity. *Nat. Mater.* **15**, 326–334 (2016).
22. G. Nowakowski, M. Dooner, H. Valinski, A. Mihaliak, P. Quesenberry, P. Becker, A specific heptapeptide from a phage display peptide library homes to bone marrow and binds to primitive hematopoietic stem cells. *Stem Cells* **22**, 1030–1038 (2004).
23. J. Zhu, S. Yang, Y. Qi, Z. Gong, H. Zhang, K. Liang, P. Shen, Y. Huang, Z. Zhang, W. Ye, L. Yue, S. Fan, S. Shen, A. Mikos, X. Wang, X. Fang, Stem cell-homing hydrogel-based miR-29b-5p delivery promotes cartilage regeneration by suppressing senescence in an osteoarthritis rat model. *Sci. Adv.* **8**, eabk0011 (2022).
24. Y. Liu, J. Chen, H. Liang, Y. Cai, X. Li, L. Yan, L. Zhou, L. Shan, H. Wang, Human umbilical cord-derived mesenchymal stem cells not only ameliorate blood glucose but also protect vascular endothelium from diabetic damage through a paracrine mechanism mediated by MAPK/ERK signaling. *Stem Cell Res. Ther.* **13**, 258 (2022).
25. C. Lin, B. Tao, Y. Deng, Y. He, X. Shen, R. Wang, L. Lu, Z. Peng, Z. Xia, K. Cai, Matrix promote mesenchymal stromal cell migration with improved deformation via nuclear stiffness decrease. *Biomaterials* **217**, 119300 (2019).
26. J. Butler, H. Kobayashi, S. Rafii, Instructive role of the vascular niche in promoting tumour growth and tissue repair by angiocrine factors. *Nat. Rev. Cancer* **10**, 138–146 (2010).
27. T. Li, H. Ma, H. Ma, Z. Ma, L. Qiang, Z. Yang, X. Yang, X. Zhou, K. Dai, J. Wang, Mussel-inspired nanostructures potentiate the immunomodulatory properties and angiogenesis of mesenchymal stem cells. *ACS Appl. Mater. Interfaces* **11**, 17134–17146 (2019).
28. N. Huebsch, P. Arany, A. Mao, D. Shvartsman, O. Ali, S. Bencherif, J. Rivera-Feliciano, D. Mooney, Harnessing traction-mediated manipulation of the cell/matrix interface to control stem-cell fate. *Nat. Mater.* **9**, 518–526 (2010).
29. R. Xu, X. Shen, Y. Si, Y. Fu, W. Zhu, T. Xiao, Z. Fu, P. Zhang, J. Cheng, H. Jiang, MicroRNA-31a-5p from aging BMSCs links bone formation and resorption in the aged bone marrow microenvironment. *Aging Cell* **17**, e12794 (2018).
30. B. Nitzsche, W. W. Rong, A. Goede, B. Hoffmann, F. Scarpa, W. M. Kuebler, T. W. Secomb, A. R. Pries, Coalescent angiogenesis-evidence for a novel concept of vascular network maturation. *Angiogenesis* **25**, 35–45 (2022).
31. I. Reid, E. Billington, Drug therapy for osteoporosis in older adults. *Lancet* **399**, 1080–1092 (2022).
32. O. Johnell, J. A. Kanis, An estimate of the worldwide prevalence and disability associated with osteoporotic fractures. *Osteoporos. Int.* **17**, 1726–1733 (2006).
33. Y. Yang, T. Xu, Q. Zhang, Y. Piao, H. P. Bei, X. Zhao, Biomimetic, stiff, and adhesive periosteum with osteogenic-angiogenic coupling effect for bone regeneration. *Small* **17**, e2006598 (2021).
34. V. Liu, P. Huang, Cardiovascular roles of nitric oxide: A review of insights from nitric oxide synthase gene disrupted mice. *Cardiovasc. Res.* **77**, 19–29 (2008).
35. Q. Zhao, J. Zhang, L. Song, Q. Ji, Y. Yao, Y. Cui, J. Shen, P. Wang, D. Kong, Polysaccharide-based biomaterials with on-demand nitric oxide releasing property regulated by enzyme catalysis. *Biomaterials* **34**, 8450–8458 (2013).
36. Y. Kanno, T. Into, C. Lowenstein, K. Matsushita, Nitric oxide regulates vascular calcification by interfering with TGF- signalling. *Cardiovasc. Res.* **77**, 221–230 (2008).
37. C. Coletta, A. Papapetropoulos, K. Erdelyi, G. Olah, K. Módis, P. Panopoulos, A. Asimakopoulou, D. Gerö, I. Sharina, E. Martin, C. Szabo, Hydrogen sulfide and nitric oxide are mutually dependent in the regulation of angiogenesis and endothelium-dependent vasorelaxation. *Proc. Natl. Acad. Sci. U.S.A.* **109**, 9161–9166 (2012).
38. S. Theivendran, Z. Gu, J. Tang, Y. Yang, H. Song, Y. Yang, M. Zhang, D. Cheng, C. Yu, Nanostructured organosilica nitric oxide donors intrinsically regulate macrophage polarization with antitumor effect. *ACS Nano* **16**, 10943–10957 (2022).
39. M. Vallet-Regí, D. Lozano, B. González, I. Izquierdo-Barba, Biomaterials against bone infection. *Adv. Healthc. Mater.* **9**, e2000310 (2020).
40. D. Jiang, C. Burger, V. Akhanov, J. Liang, R. Mackin, N. Albrecht, P. Andrade, D. Schafer, M. Samuel, Neuronal signal-regulatory protein alpha drives microglial phagocytosis by limiting microglial interaction with CD47 in the retina. *Immunity* **55**, 2318–2335.e17 (2022).
41. R. Hsu, S. Li, J. Fang, I. Lee, L. Chu, Y. Lo, Y. Lu, Y. Chen, S. Hu, Wireless charging-mediated angiogenesis and nerve repair by adaptable microporous hydrogels from conductive building blocks. *Nat. Commun.* **13**, 5172 (2022).
42. Z. Dou, H. Tang, K. Chen, D. Li, Q. Ying, Z. Mu, C. An, F. Shao, Y. Zhang, Y. Zhang, H. Bai, G. Zheng, L. Zhang, T. Chen, H. Wang, Highly elastic and self-healing nanostructured gelatin/clay colloidal gels with osteogenic capacity for minimally invasive and customized bone regeneration. *Biofabrication* **15**, 025001 (2023).
43. J. Su, H. Sun, Q. Meng, P. Zhang, Q. Yin, Y. Li, Enhanced blood suspensibility and laser-activated tumor-specific drug release of theranostic mesoporous silica nanoparticles by functionalizing with erythrocyte membranes. *Theranostics* **7**, 523–537 (2017).
44. C. Lin, K. Xu, Y. He, B. Tao, Z. Yuan, K. Li, X. Li, Z. Xia, K. Cai, A dynamic matrix potentiates mesenchymal stromal cell paracrine function via an effective mechanical dose. *Biomater. Sci.* **8**, 4779–4791 (2020).
45. M. Darnell, L. Gu, D. Mooney, RNA-seq reveals diverse effects of substrate stiffness on mesenchymal stem cells. *Biomaterials* **181**, 182–188 (2018).
46. E. Baxter, A. Graham, N. Re, I. Carr, J. Robinson, S. Mackie, A. Morgan, Standardized protocols for differentiation of THP-1 cells to macrophages with distinct M(IFNγ+LPS), M(IL-4) and M(IL-10) phenotypes. *J. Immunol. Methods* **478**, 112721 (2020).
47. W. Cui, X. Wu, Y. Shi, W. Guo, J. Luo, H. Liu, L. Zheng, Y. Du, P. Wang, Q. Wang, D. Feng, S. Ge, Y. Qu, 20-HETE synthesis inhibition attenuates traumatic brain injury-induced

mitochondrial dysfunction and neuronal apoptosis via the SIRT1/PGC-1α pathway: A translational study. *Cell Prolif.* **54**, e12964 (2021).

48. X. He, D. Wang, P. Chen, Y. Qiao, T. Yang, Z. Yu, C. Wang, H. Wu, Construction of a novel "ball-and-rod" MSNs-pp-PEG system: A promising antitumor drug delivery system with a particle size switchable function. *Chem. Commun.* **56**, 4785–4788 (2020).